

Topological band structure via twisted photons in a degenerate cavity

Mu Yang^{1,2,3}, Hao-Qing Zhang^{1,2,3}, Yu-Wei Liao^{1,2,3}, Zheng-Hao Liu^{1,2}, Zheng-Wei Zhou^{1,2}, Xing-Xiang Zhou^{1,2}, Jin-Shi Xu^{1,2}, Yong-Jian Han^{1,2}, Chuan-Feng Li^{1,2} & Guang-Can Guo^{1,2}

Synthetic dimensions based on particles' internal degrees of freedom, such as frequency, spatial modes and arrival time, have attracted significant attention. They offer ideal large-scale lattices to simulate nontrivial topological phenomena. Exploring more synthetic dimensions is one of the paths toward higher dimensional physics. In this work, we design and experimentally control the coupling among synthetic dimensions consisting of the intrinsic photonic orbital angular momentum and spin angular momentum degrees of freedom in a degenerate optical resonant cavity, which generates a periodically driven spin-orbital coupling system. We directly characterize the system's properties, including the density of states, energy band structures and topological windings, through the transmission intensity measurements. Our work demonstrates a mechanism for exploring the spatial modes of twisted photons as the synthetic dimension, which paves the way to design rich topological physics in a highly compact platform.

¹CAS Key Laboratory of Quantum Information, University of Science and Technology of China, Hefei 230026, PR China. ²CAS Center For Excellence in Quantum Information and Quantum Physics, University of Science and Technology of China, Hefei 230026, PR China. ³These authors contributed equally: Mu Yang, Hao-Qing Zhang and Yu-Wei Liao. ✉email: jsxu@ustc.edu.cn; smhan@ustc.edu.cn; cfl@ustc.edu.cn

The dimensions of physical models simulated by real space lattices, such as photonic crystals^{1–3}, metamaterials⁴ and microcavity arrays⁵, are generally smaller than or equal to their geometric dimensions. Great efforts have been made to simulate high-dimensional physics. Recently, a powerful approach by introducing synthetic dimensions to the lower geometric dimensions with remarkably fewer experimental requirements has caused increasing interest^{6,7}. The $(D + d)$ -dimensional physics can be investigated in D geometric dimensions with d synthetic dimensions. The synthetic dimensions could be formed by the particles' internal degrees of freedom in photonic^{6,8} or atomic systems^{9–11}.

Abundant topological phenomena have been demonstrated through utilizing the photonic frequencies^{12–15}, optical waveguide modes¹⁶ and optical pulse arrival time^{17,18} as synthetic physical dimensions. Exploring more synthetic dimensions is helpful to investigate higher dimensional physics.

Photonic orbital angular momentum (OAM) with infinite topological charge numbers is an ideal degree of freedom for constructing the synthetic lattice. The photons carrying OAM have twisted wavefronts, referred to as twisted photons¹⁹. Moreover, optical systems with a tunable coupling between the intrinsic spin angular momentum (SAM) and the synthetic OAM dimension of photons offer natural platforms to simulate the topological physics in spin-orbital coupling (SOC) systems. As the first proposal for synthetic dimensions^{7,8}, degenerate optical cavities simultaneously support plenty of OAM modes have been employed in theoretical protocols to simulate a wide variety of topological physics including the non-Abelian gauge fields induced phase transition²⁰ and edge states²¹. The synthetic frequency and OAM dimensions are combined in a single cavity to investigate gauge field physics²². Multimode optical cavities have also been experimentally used to simulate Landau levels^{23,24}, which are the first two-dimensional topological cavity, and have also been used to engineer Hamiltonians²⁵. However, there has been no experimental demonstration of the OAM degenerate cavity-assisted SOC physics until now.

In this work, we develop an extremely compact platform and experimentally investigate the properties of a periodically driven SOC topological system in a degenerate optical cavity with the photonic OAM serving as a synthetic dimension. The coupling between the synthetic dimension and its internal spin is well constructed. By detecting the transmission intensity of the degenerate cavity, we directly obtain the density of states (DOS), energy band structures, and topological windings of the simulated system. Although some topological evidences have been demonstrated through quantum walk on OAM modes in stackable systems^{26–28}, the direct band observations are not available. Our experiments open the door to directly explore high-dimensional topological physics with synthetic dimensions in a simple system.

Results

Theoretical framework. The degenerate optical cavity shown in Fig. 1a consists of two high reflective plane mirrors and two convex lenses. The input optical mode locates one focal length (f) in front of the first lens while the output optical mode locates one focal length after the second lens, which forms an exact $4f$ system. See Supplementary Fig. S1 for details of experimental setup. The cavity can stabilize more than 10^3 photonic OAM modes (see section I of Supplementary Information (SI) for more details), which steadily reproduce themselves periodically since they go through the precise $4f$ telescope once every period. A large synthetic lattice based on OAM modes can then be constructed in the optical degenerate cavity. The degenerate cavity carrying a variety of OAM modes requires the precise control of surface quality and position of cavity elements. Aberrations may destroy its degeneracy^{29–31}, which implies that the experimental requirement is high. We pursue this kind of degeneracy to reduce the self-energy disorder in the cavity which may destroy the topological character in the system.

The generation of high-order spatial OAM modes with the input Gaussian mode and the coupling between the OAM and SAM modes are simultaneously achieved via an anisotropic and inhomogeneous medium (named Q-plate³²) in the cavity (see Methods). The action of the Q-plate ($J_{Q(\delta)}$) is described as:

$$J_{Q(\delta)} = \sum_m \cos(\delta/2) (a_{\mathcal{O},m}^\dagger a_{\mathcal{O},m} + a_{\mathcal{O},m}^\dagger a_{\mathcal{O},m}) + i \sin(\delta/2) (a_{\mathcal{O},m+2q}^\dagger a_{\mathcal{O},m} + \text{h.c.}), \quad (1)$$

where m represents the topological charge numbers of OAM modes with corresponding twisted wavefronts; $\mathcal{O}(\mathcal{O})$ denotes the left (right)-circular polarized SAM modes; $a_{\mathcal{O}(\mathcal{O}),m}^\dagger$ ($a_{\mathcal{O}(\mathcal{O}),m}$) is the corresponding creation (annihilation) operator; q is the topological charge number of the Q-plate and $q = 1$ in our experiment; and δ is the value of the optical retardation which can be tuned by the applied electric field. To manipulate the optical SAM modes, an additional wave plate (WP) with the operation of $J_{\lambda(\eta)} = \sum_m \cos(\eta) (a_{\mathcal{O},m}^\dagger a_{\mathcal{O},m} + a_{\mathcal{O},m}^\dagger a_{\mathcal{O},m}) + i \sin(\eta) (a_{\mathcal{O},m}^\dagger a_{\mathcal{O},m} + \text{h.c.})$ is introduced in the cavity. The control parameter η represents the phase retardance between ordinary and extraordinary photons, which is determined by the WP's thickness (e.g., $\eta = \pi/4$ for a quarter-wave plate (QWP)). When the Q-plate and WP are introduced in the cavity, the position and orientation of the cavity should be re-optimized to maintain the degenerate property.

The optical state in the cavity is evolved under the periodic unitary: $\hat{U}(\delta, \eta) = J_{Q(\delta)} J_{\lambda(\eta)} J_{\lambda(\eta)} J_{Q(\delta)}$ which is an one round trip including both the actions of the Q-plate and WP. Due to its periodicity, an effective Hamiltonian \hat{H}_{eff} can be introduced as

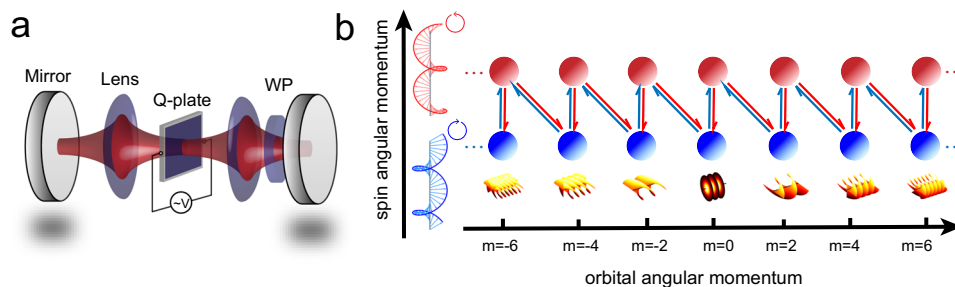


Fig. 1 Experimental setup and the coupling model. **a** The degenerate cavity consists of two plane mirrors and two lenses. High-order photonic modes are generated and coupled by repeatedly passing an anisotropic and inhomogeneous medium (Q-plate) and a wave plate (WP) with an input Gaussian mode. **b** Schematic of spin and lattice for SAM and OAM modes. The SAM modes with left (\mathcal{O}) and right (\mathcal{O}) circular polarizations are labeled in red and blue, respectively. The OAM modes are marked as the arrays of balls. The corresponding twisted wavefronts are shown below the coupling modes.

$\hat{U}(\delta, \eta) = e^{-i\hat{H}_{\text{eff}}T/\hbar}$, where $T = L/c$, with L being the one round trip (one period) length of the cavity and c representing the speed of light, denotes the period of a round-trip. The average lifetime of photons in the cavity is about $5T$, which means the photons pass through the Q-plate 10 times on average (see section I of SI for more details). The operation of $\hat{U}(\delta, \eta)$ drives the hopping among SAM and OAM modes (shown in Fig. 1b), which shares the features of the simplest topological lattice Su-Schrieffer-Heeger (SSH) model³³ in the Floquet version. As a result, the stable optical state $|\phi(t)\rangle$ at time t , which is a superposition state of SAM and OAM modes ($|\mathcal{O}(\mathcal{O}), m\rangle$), is evolved as $|\phi(t+T)\rangle = e^{-i\hat{H}_{\text{eff}}T/\hbar}|\phi(t)\rangle$. From the point of view of the self-reproductive condition, the stable optical states in the degenerate cavity satisfies: $|\phi(t+T)\rangle = e^{-i\beta L}|\phi(t)\rangle$. $\beta = 2\pi/\lambda + i\alpha$ is independent of SAM and OAM modes. λ represents the wavelength of the photons in the cavity and α is the attenuation coefficient. Combining the evolution and the reproductive conditions of the optical state in the degenerate cavity, we obtain

$$e^{-i\hat{H}_{\text{eff}}T/\hbar}|\phi(t)\rangle = e^{-i\beta L}|\phi(t)\rangle. \quad (2)$$

As a consequence, the stable photonic state $|\phi\rangle$ (t is omitted) in the degeneracy cavity is naturally the eigenstates of \hat{H}_{eff} with eigenvalues βL (taking $T/\hbar = 1$).

Since the Q-plate and WP have same operational forms on different m , there should not be disorders in the coupling and the effective Hamiltonian \hat{H}_{eff} possesses translational symmetry on m . As a result, if we introduce the Bloch mode $|k\rangle$ in ‘momentum’ space as $|k\rangle = \sum_j e^{-ijk}|j\rangle$ ($j = m/2$), the Hamiltonian can be recast in the ‘quasi-momentum’ space as $\hat{H}_{\text{eff}} = \int_{-\pi}^{\pi} \hat{H}_{\text{eff}}(k)dk$, where $\hat{H}_{\text{eff}}(k) = E_k \mathbf{n}(k) \cdot \boldsymbol{\sigma}|k\rangle\langle k|$. E_k represents the dispersion relation, $\boldsymbol{\sigma} = (\sigma_x, \sigma_y, \sigma_z)$ is the Pauli vector and $\mathbf{n}(k) = [n_x(k), n_y(k), n_z(k)]$ is a unit vector. The eigenstate of $\hat{H}_{\text{eff}}(k)$ can be represented as $|\phi_k^s\rangle = |\psi_k^s\rangle|k\rangle$, where $|\psi_k^s\rangle$ is the eigenstate of operator $\mathbf{n}(k) \cdot \boldsymbol{\sigma}$ and $s = \pm 1$ represents the band index. At the parameter range of $-\pi \leq k \leq \pi$, the eigenenergy of $\hat{H}_{\text{eff}}(k)$ forms two symmetrical energy bands with $\pm E_k$. In our experiment, this system possesses the chiral symmetry, since $\hat{H}_{\text{eff}}(k)$ satisfies $\Gamma \hat{H}_{\text{eff}}(k) \Gamma = -\hat{H}_{\text{eff}}(k)$ with $\Gamma = \sigma_z$ (see section II of SI for more details).

Interestingly, the eigenstates of \hat{H}_{eff} can be directly obtained by measuring the transmission intensities of the cavity. Since the eigenstates of \hat{H}_{eff} form a complete basis, the output state of the cavity could be expanded as $|\phi_{\text{out}}\rangle = \sum_{k,s} T_k^s |\phi_k^s\rangle$. According to the input-output relation of the cavity (see section III of SI for more details), the transmission amplitude can be expressed as

$$T_k^s = \frac{|\kappa|^2/r}{1 - r e^{-i(sE_k - \beta\Delta L)}} \langle \phi_k^s | \phi_{\text{in}} \rangle. \quad (3)$$

ΔL denotes the cavity’s detuning which equals to $L - 2n\pi/\beta(n \in \mathbb{N}^+)$. κ and r are the coupling and reflection coefficients respectively of the cavity and they satisfy the condition that $|\kappa|^2 + |r|^2 = 1$, which are nearly same for different OAMs. By choosing an appropriate input state $|\phi_{\text{in}}\rangle$, $\sum_s |\langle \phi_k^s | \phi_{\text{in}} \rangle|^2$ could be independent on k (see section III of SI for more details). The whole output transmission intensity, which can be directly measured, is defined as $I_o = \sum_{k,s} |T_k^s|^2$. We can find that in Eq. 3, only when the term $\beta\Delta L$ is closest to sE_k , the photonic output state $|\phi_{\text{out}}\rangle$ is closest to the eigenstate $|\phi_k^s\rangle$ and the relevant I_o reaches its local maximum at the same time (see Supplementary Fig. S2 in section IV of SI for more details). Moreover, the transmission intensity I_o contributed

by all eigenstate $|\phi_k^s\rangle$ of all k corresponds to the density of state (DOS) under renormalization (see section III of SI for more details).

Experimental results. From the spectrum of DOS, the energy gap of the system with the zero DOS can also be directly read out. In our experiments, the parameter η can be used to control the coupling strength between SAM modes and the m -th OAM mode. If $\eta = 0$ (there is no WP in the cavity), there is no coupling between $|\mathcal{O}, m\rangle$ and $|\mathcal{O}, m\rangle$ and the simulated system is reduced to a two-level system. The hopping occurs only between photonic angular momentum states $|\mathcal{O}, m\rangle$ and $|\mathcal{O}, m+2\rangle$, as shown in Fig. 2a. The measured full spectrum of DOS as a function of δ and $\beta\Delta L$ is shown in Fig. 2b, and the special cases with $\delta = 0$ (closing gap) and $\delta = \pi/8$ (opening gap) are shown in the top and bottom panels of Fig. 2c (the band gap areas are marked in gray), respectively. The closing and opening of energy gap are dependent on the parameter of δ .

With the increase of the parameter η , the states $|\mathcal{O}, m\rangle$ and $|\mathcal{O}, m\rangle$ will couple to each other. As a result, the spin-orbital like interaction in the system can be realized with addition coupling between $|\mathcal{O}, m\rangle$ and $|\mathcal{O}, m+2\rangle$ controlled by δ , as is shown in Fig. 2d. In such kind of situation, the topological phases appear and are protected by the band gap. The closing of the gap indicates the phase transition between the topological phase and the trivial phase. The measured full spectrum of DOS as function of δ with $\eta = \pi/8$ (the WP is an eighth-wave plate in the cavity) is shown in Fig. 2e. The band gap closes at $\delta = \pm\pi/8$ and $\delta = \pm 3\pi/8$ which indicate two phase transitions. In Fig. 2f, the DOS with the gap closing at $\delta = \pi/8$ (top panel) is further compared with the gap opening at $\delta = \pi/4$ (bottom panel). The spectrum of DOS as function of δ with another $\eta = \pi/4$ (the WP is a QWP in cavity) is shown in Fig. 2h. The schematic SOC interaction is shown in Fig. 2g. Similarly, there are two gap closure points at $\delta = \pm\pi/4$ ^{27,28} and the comparison of DOS with the gap closing at $\delta = \pi/4$ (top panel) and with the gap opening at $\delta = \pi/8$ (bottom panel) is shown in Fig. 2i. Worthy to note that our system only has topological protection versus disorder in the coupling constants but not between disorder in the self-energy. The slight deformity of the spectra in Figs. 2c, f, i illustrate a distribution of energies around the main energy, which may be due to the imperfect degeneracy of the cavity.

The spectra of DOS display the number of states with the same energy. However, the degeneracy of energy ($E_{-k} = E_k$) leads to the indistinguishability of the states with momentum k and $-k$. To determine the relationship between the quasienergy E_k and the quasimomentum k , which characterizes the corresponding band structure of the SOC system, we should scan the transmission intensity $I_k = \sum_s |T_k^s|^2$ as a function of a post-selected Bloch momentum state $|k\rangle$ (see section V of SI for more details). In experiment, the state projection is carried out by a spatial light modulator (SLM). The state $|k\rangle$ with a superposition of OAM modes is transferred to the Gaussian mode with $m = 0$ that is determined by a single mode fiber. However, due to the limitation of the SLM’s spatial resolution, we can only project the output state onto $|k_{\text{exp}}\rangle = \sum_{j=-N/2}^{j=N/2} e^{-ijk_{\text{exp}}}|j\rangle$ ($j = m/2$) with N setting to 12. $|k_{\text{exp}}\rangle$ approaches to $|k\rangle$ when N increases to infinity. The detailed projection process can be found in Methods and the photon distributions (Supplementary Fig. S3) after the SLM’s modulation are shown in section VI of SI.

The representative theoretical and experimental band structures with different δ (0, $\pi/12$ and $\pi/6$) at $\eta = \pi/4$ are shown in Fig. 3. Note that due to the limited N ($N = 12$), the obtained transmission intensity is a bit concentrated at $k_{\text{exp}} = 0$ and π . With the improvement of the spatial resolution of SLM, the experimental results will approach to the ideal results by increasing N . Since the

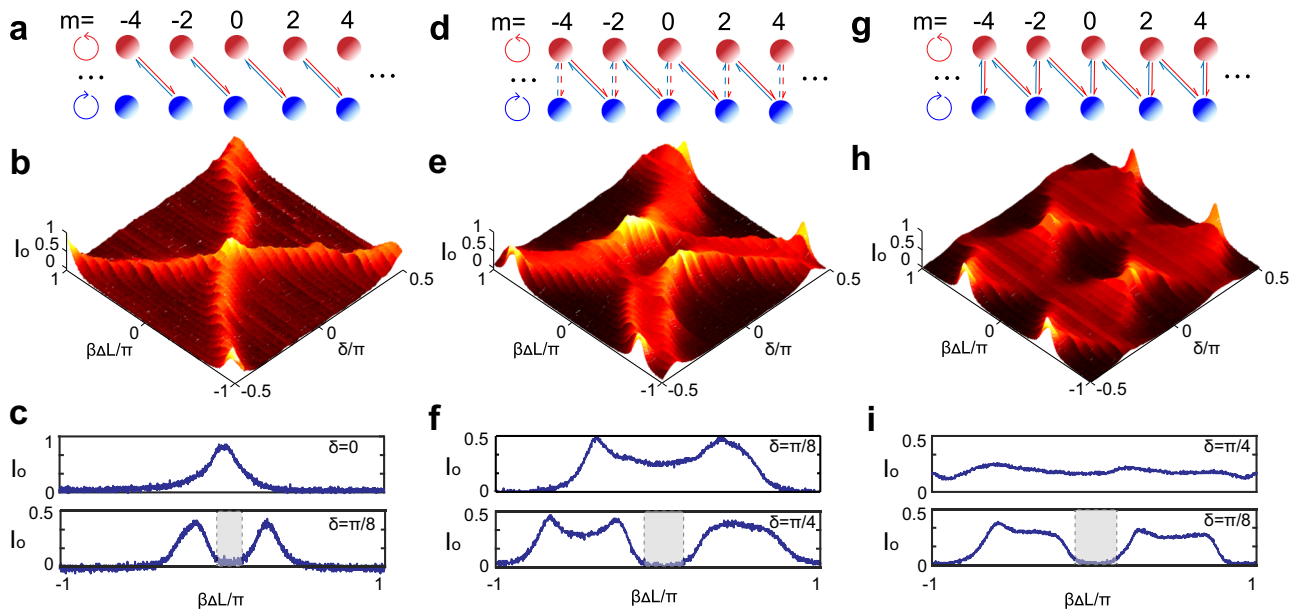


Fig. 2 detected photonic density of state (DOS) in (η, δ) space. **a, d, and g** The coupling among the photonic angular momentum with $\eta = 0, \pi/8, \pi/4$, respectively. The coupling of SAM modes with different η are denoted as no lines, dashed lines and solid lines between nearby modes, respectively. **b, e, and h** The normalized transmission intensity as a function of the normalization cavity detuning parameters $\beta\Delta L/\pi$ and δ/π . **c, f, and i** The spectra of DOS when the gap closes and opens at different δ . The band gap areas are marked in gray.

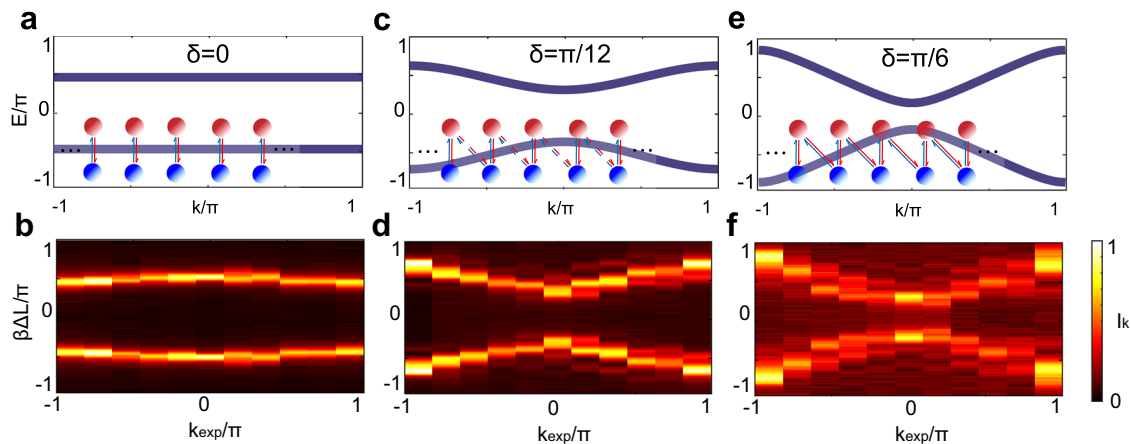


Fig. 3 Theoretical and experimental band structures. **a, c, and e** Theoretically calculated energy band spectra with $\delta = 0, \pi/12$ and $\pi/6$ when $\eta = \pi/4$, respectively. The x (y)-axis represents the normalized quasimomentum k/π (quasienergy E_k/π). The coupling among optical angular momentum are shown in the inserts, in which the increasing strength is denoted as no lines, dashed lines and solid lines between nearby modes, respectively. **b, d, and f** The corresponding experimental energy band of $\delta = 0, \pi/12$, and $\pi/6$ when $\eta = \pi/4$, respectively. The x (y)-axis represents the normalized cavity detuning $\beta\Delta L/\pi$ (the parameter k_{exp}/π).

band structure represents the refined DOS, the band gap of the simulated topological system also can be read out directly.

It is well known that the SOC systems exhibiting different topological phases can be distinguished by their winding numbers. According to the intrinsic chiral symmetry determined by the form of the unitary operation $\hat{U}(\delta, \eta)$ in one period, the topological bulk invariant in such system can be defined by the winding number of the unit vector $\mathbf{n}(k)$ in Hamiltonian \hat{H}_{eff} . The vector $\mathbf{n}(k)$ winds around a fixed axis z with varying k and the trajectory forms a circle on the Bloch sphere. Through performing the polarization Pauli measurements of σ_i ($i = x, y, z$) on the post-selected state $|k\rangle$, the transmission intensity I_k is modified to $I_k^i = \sum_s s n_i(k) |T_k^s|^2$. Therefore, the unit vector $\mathbf{n}(k)$ and the corresponding winding number can be derived from the variation of the transmission peaks (see section VII of SI for more details).

For a periodic driving system, its topological phases should be characterized by two different timeframes (different sequences of the operations in the cavity)^{34,35}. The different timeframes give the same dispersion relationship but different windings of the unit vector $\mathbf{n}(k)$, which correspond to different topologies (see section II of SI for more details). For the 1st timeframe in Fig. 4a, the evolution operation is $\hat{U}(\delta, \eta) = J_{Q(\delta)} J_{\lambda(\eta)} J_{\lambda(\eta)} J_{Q(\delta)}$. By choosing the parameters to be $\delta = \pi/2$ and $\eta = \pi/4$, the experimental (top panel) and numerical (bottom panel) transmission intensities I_k^{x+} by projecting the SAM mode to the horizontal polarization state $(|\odot\rangle + |\oslash\rangle)/\sqrt{2}$ representing the eigenstate of σ_x with eigenvalue $+1$, are shown in Fig. 4b.

Different from the transmission intensity I_k in Fig. 3b (which is homogeneous along k), the normalized height of the transmitted peaks of I_k^{x+} is periodically modulated along k and exhibit the

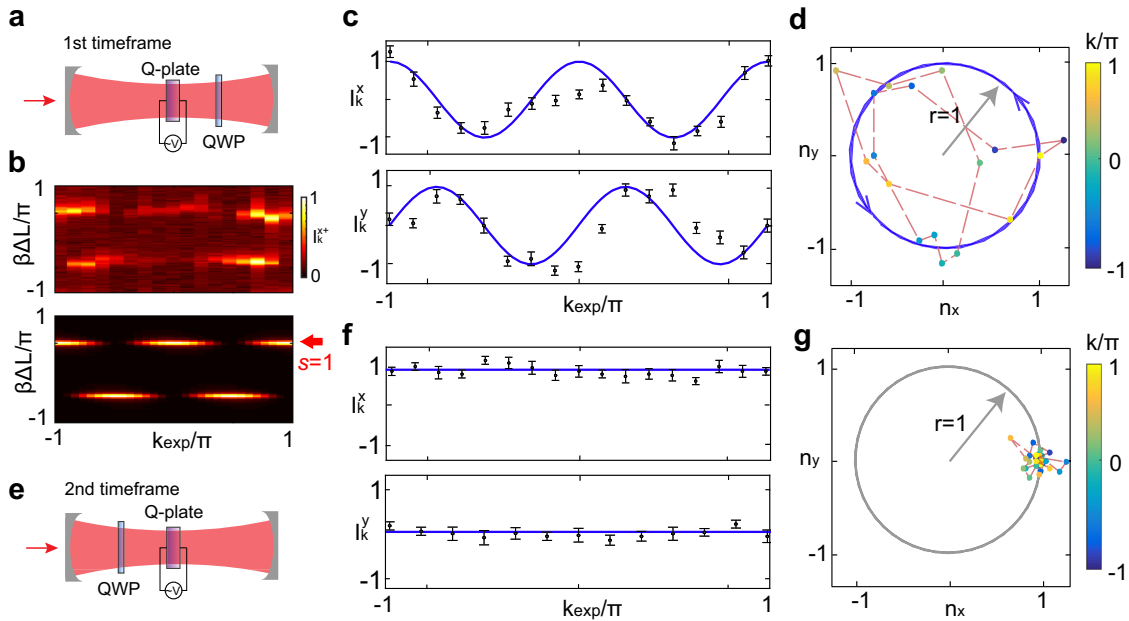


Fig. 4 Experimental windings. **a, e** Experimental setups of the 1st and 2nd timeframe settings, respectively. The parameters are set to be $\delta = \pi/2$ for the Q-plate and $\eta = \pi/4$ for the QWP. **b.** The experimentally measured (top) and numerically simulated (bottom) transmission intensities I_k^{x+} on the horizontal polarization state $(| \uparrow \rangle + | \circ \rangle) / \sqrt{2}$ along the quasimomentum k_{exp} . The unit vector $\mathbf{n}(k)$ are readout according to $\beta\Delta L > 0$ with $s = 1$. **c, f** The normalized transmitted peaks on basis σ_x (top) and σ_y (bottom) of the 1st and 2nd timeframes. The black dots represent the experimental data while the blue curves represent the theoretical predictions. **d, g** The topological windings of measured (n_x, n_y) at the 1st and 2nd timeframes. The blue circle with the radius of $r = 1$ represent the theoretical predictions.

variations of $sn_x(k)$. Furthermore, the height of the transmitted peaks as a function of the quasimomentum k can be divided into two complementary parts: one is for $\beta\Delta L > 0$ corresponding to the upper band ($s = 1$), and the other is for $\beta\Delta L < 0$ corresponding to the lower band ($s = -1$). Since $\mathbf{n}(k)$ in each band defines the same winding number, without loss of generality, we choose the upper band to calculate the topological winding number.

We further detect the normalized height of the transmitted peaks of I_k^{x-} by projecting the SAM mode of the output photons to the vertical state $(| \uparrow \rangle - | \circ \rangle) / \sqrt{2}$, which is the eigenstate of σ_x with eigenvalue -1 . The value of $n_x(k)$ is determined by $I_k^x = I_k^{x+} - I_k^{x-}$ and the corresponding experimental results are shown in Fig. 4c (upper panel). The value of $n_y(k)$ can be determined by $I_k^y = I_k^{y+} - I_k^{y-}$, where I_k^{y+} and I_k^{y-} represent the normalized height of the transmitted peaks by projecting the SAM modes to $(| \uparrow \rangle - i| \circ \rangle) / \sqrt{2}$ and $(| \uparrow \rangle + i| \circ \rangle) / \sqrt{2}$, respectively. The experimental results are shown in the lower panel of Fig. 4c. Error bars are estimated according to the fluctuation of the output intensities.

In the $x - y$ plane, we find that the normalized vector $[n_x(k), n_y(k)]$ winds twice anticlockwise around the chiral axis as the quasimomentum k traverses in the first Brillouin zone $[-\pi, \pi]$. The corresponding experimental result is shown in Fig. 4d, which indicates that the SOC system possesses a nontrivial topology phase in the 1st timeframe with $\delta = \pi/2$ and $\eta = \pi/4$. The nontrivial topological insulator would support edge states at interfaces where the topological invariant changes. For instance, when the coupling between SAM breaks at the center of the lattice ($m = 0$) with some unique designs (see section VIII of SI and Supplementary Fig. S4 for more details), the interface between the nontrivial topological bulk and “vacuum” can support edge states. It is worth mentioning that the winding numbers are protected by symmetry when the strength of the disorder is less than the bandgap. However, the increasing disorder can move the edge to the bulk bands.

On the other hand, the 2nd timeframe, with the evolution unitary $\hat{U}'(\delta, \eta) = J_{\lambda(\eta)} J_{Q(\delta)} J_{Q(\delta)} J_{\lambda(\eta)}$, is constructed by exchanging the Q-plate and WP in the cavity, which is shown in Fig. 4e. The corresponding experimental results of $n_x(k)$ and $n_y(k)$ are shown in Fig. 4f. In the $x - y$ plane, $\mathbf{n}(k)$ winds 0 round in Fig. 4g. As a result, although the SOC system in both timeframes have the same band structure, they have completely different winding numbers.

Discussion

In conclusion, we have experimentally demonstrated a compact optical spin-orbital coupling system in a degenerate cavity. The optical OAM degree of freedom serves as a synthetic dimension, and the interaction strength of SOC, introduced by the Q-plate and WP in the cavity, can be tuned conveniently. The DOS, band structures, and topological windings of the synthetic topological insulator, which shares the famous features of SSH model, are directly obtained by detecting the transmission intensity of the cavity. Through manipulating the parameters of the cavity, we obtain multiple DOS to observe the closing of the band gap directly and investigate the topological phases in different time frames.

Our work provides a versatile platform based on an OAM degenerate cavity to explore richer topological physics. Higher-dimensional physics can then be exploited in the compact platform. The 2-leg ladder model can be achieved by introducing an additional Q-plate with $q = -1$ into the cavity. Moreover, the setup is compatible with other synthetic dimensions, including the frequency degree of freedom²². By introducing the external gauge fields in the cavity, topological systems with the famous Hofstadter’s butterfly spectrum can be directly investigated²⁰. Two-dimensional topological systems are generally more robust than one-dimensional topological systems. The topological properties of one-dimensional systems come purely from

symmetries, while the topological properties of two-dimensional systems come from gauge fields.

Moreover, non-Hermitian interactions would be realized through involving the gain/loss of the spin degree of freedom in the cavity and the non-Hermitian physics can also be well-studied^{36,37}. The introduced nonlinearities or gain/loss would create “boundaries” inside the bulk and make the topological systems without boundaries still present topological bulk properties. The degenerate cavity containing many optical angular momentum may also suit for employing as all-optical devices, such as quantum memory and optical filters³⁸.

Methods

The operation of Q-plate. The Q-plate is composed of liquid crystal molecules with different optical axes, each of which is equivalent to a half-wave plate³². The optical axis of cylindrical coordinate satisfies

$$\alpha(r, \phi) = q\phi, \quad (4)$$

where q are constants. The Jones formalism of Q-plate M_Q can be written as

$$M_Q = \cos(\delta/2)\mathbf{I} + i \sin(\delta/2) \begin{bmatrix} \cos 2\alpha & \sin 2\alpha \\ \sin 2\alpha & -\cos 2\alpha \end{bmatrix}, \quad (5)$$

where δ is the optical retardation and is controlled by the applied electric field. Within the paraxial approximation, a left (right)-circular polarized plane wave

$E = E_0 \begin{bmatrix} 1 \\ \pm i \end{bmatrix} e^{im\phi}$, denoted as $|\mathcal{O}(\mathcal{C}), m\rangle$ (where $\mathcal{O}(\mathcal{C})$ denotes the left (right)-circular polarized SAM modes and m is the topological charge of OAM, passes through the Q-plate, and the plane wave would change to

$$\frac{E'}{E_0} = \cos(\delta/2) \begin{bmatrix} 1 \\ \pm i \end{bmatrix} + i \sin(\delta/2) e^{i[(\pm 2q+m)\phi]} \begin{bmatrix} 1 \\ \mp i \end{bmatrix}. \quad (6)$$

The vortex phase $e^{\pm i2q\phi}$ (topological charge is $2q$) is introduced during the spin-to-orbital angular momentum conversion.

The phase hologram. Within the paraxial approximation, the state $|m\rangle$ of the photon carrying OAM with topological charge m can be approximately expressed as

$$|m\rangle = E_0 e^{im\phi}, \quad (7)$$

where the phase $\phi = \tan^{-1}(y/x)$ in cartesian coordinates (x, y) . The phase of $|k_{\text{exp}}\rangle$ at the position of (x, y) is

$$\begin{aligned} \varphi_{(k_{\text{exp}}, N)}(x, y) &= \arg \sum_{j=-N/2}^{j=N/2} e^{-ijk_{\text{exp}}} |j\rangle \\ &= \arg \sum_{m=-N}^{m=N} e^{-im(k_{\text{exp}}/2+\phi)}, \end{aligned} \quad (8)$$

where $j = m/2$. For an 8-bit SLM, the modulation phase from 0 to 2π is mapped to gray value 0 to 255. The hologram of basis $|k_{\text{exp}}\rangle \langle k_{\text{exp}}|$ is given by

$$H_{(k_{\text{exp}}, N)}(x, y) = [\text{mod}(\varphi_{(k_{\text{exp}}, N)}(x, y), 2\pi) \times 255], \quad (9)$$

where $H_{(k_{\text{exp}}, N)}(x, y)$ represents the gray value at (x, y) position on SLM. The hologram $H_{(k_{\text{exp}}, N)}(x, y)$ on SLM is parameterized by (k_{exp}, N) .

Data availability

All of the data supporting the conclusions are available within the article and the Supplementary Information. Additional data are available from the corresponding authors upon reasonable request.

Received: 21 September 2021; Accepted: 28 March 2022;

Published online: 19 April 2022

References

- Joannopoulos, J., Villeneuve, P. & Fan, S. Photonic crystals: putting a new twist on light. *Nature* **386**, 143 (1997).
- Lu, L. et al. Experimental observation of Weyl points. *Science* **349**, 622–624 (2015).
- Zhou, H. et al. Observation of bulk Fermi arc and polarization half charge from paired exceptional points. *Science* **359**, 1009–1012 (2018).

- Soukoulis, C. & Wegener, M. Past achievements and future challenges in the development of three-dimensional photonic metamaterials. *Nat. Photon.* **5**, 523 (2011).
- Ota, Y. et al. Active topological photonics. *Nanophotonics* **9**, 547 (2020).
- Yuan, L., Lin, Q., Xiao, M. & Fan, S. Synthetic dimension in photonics. *Optica* **5**, 1396–1405 (2018).
- Ozawa, T. & Price, H. M. Topological quantum matter in synthetic dimensions. *Nat. Rev. Phys.* **1**, 349–357 (2019).
- Ozawa, T. et al. Topological photonics. *Rev. Mod. Phys.* **91**, 015006 (2019).
- Jotzu, G. et al. Experimental realization of the topological Haldane model with ultracold fermions. *Nature* **515**, 237–240 (2014).
- Boada, O., Celi, A., Latorre, J. I. & Lewenstein, M. Quantum simulation of an extra dimension. *Phys. Rev. Lett.* **108**, 133001 (2012).
- Kraus, Y. E., Ringel, Z. & Zilberberg, O. Four-dimensional quantum Hall effect in a two-dimensional quasicrystal. *Phys. Rev. Lett.* **111**, 226401 (2013).
- Dutt, A. et al. A single photonic cavity with two independent physical synthetic dimensions. *Science* **367**, 59–64 (2020).
- Dutt, A. et al. Experimental band structure spectroscopy along a synthetic dimension. *Nat. Commun.* **10**, 1–8 (2019).
- Li, G. et al. Dynamic band structure measurement in the synthetic space. *Sci. Adv.* **7**, 4335 (2021).
- Wang, K. et al. Generating arbitrary topological windings of a non-Hermitian band. *Science* **371**, 1240–1245 (2021).
- Lustig, E. et al. Photonic topological insulator in synthetic dimensions. *Nature* **567**, 356 (2019).
- Schreiber, A. et al. A 2D quantum walk simulation of two-particle dynamics. *Science* **336**, 55–58 (2012).
- Regensburger, A., Bersch, C., Miri, M., Onishchukov, G., Christodoulides, D. N. & Peschel, U. Parity-time synthetic photonic lattices. *Nature* **488**, 167–171 (2012).
- Molina-Terriza, G., Torres, J. & Torner, L. Twisted photons. *Nature Phys.* **3**, 305–310 (2007).
- Luo, X. W. et al. Quantum simulation of 2D topological physics in a 1D array of optical cavities. *Nat. Commun.* **6**, 1–8 (2015).
- Zhou, X. Dynamically manipulating topological physics and edge modes in a single degenerate optical cavity. *Phys. Rev. Lett.* **118**, 083603 (2017).
- Yuan, L. et al. Photonic gauge potential in one cavity with synthetic frequency and orbital angular momentum dimensions. *Phys. Rev. Lett.* **112**, 083903 (2019).
- Schine, N., Ryou, A., Gromov, A., Sommer, A. & Simon, J. Synthetic Landau levels for photons. *Nature* **534**, 671–675 (2016).
- Clark, L. W., Schine, N., Baum, C., Jia, N. & Simon, J. Observation of Laughlin states made of light. *Nature* **582**, 41–45 (2020).
- Rechcińska, K. et al. Engineering spin-orbit synthetic Hamiltonians in liquid-crystal optical cavities. *Science* **366**, 727–730 (2019).
- Cardano, F. et al. Quantum walks and wavepacket dynamics on a lattice with twisted photons. *Sci. Adv.* **1**, 1500087 (2015).
- Cardano, F. et al. Statistical moments of quantum-walk dynamics reveal topological quantum transitions. *Nat. Commun.* **7**, 1–8 (2016).
- Cardano, F. et al. Detection of Zak phases and topological invariants in a chiral quantum walk of twisted photons. *Nat. Commun.* **8**, 1–7 (2017).
- Cheng, Z. D. et al. Degenerate cavity supporting more than 31 Laguerre Gaussian modes. *Opt. Lett.* **42**, 2042–2045 (2017).
- Cheng, Z. D. et al. Experimental implementation of a degenerate optical resonator supporting more than 46 Laguerre-Gaussian modes. *Appl. Phys. Lett.* **112**, 201104 (2018).
- Cheng, Z. D. et al. Flexible degenerate cavity with ellipsoidal mirrors. *Opt. Lett.* **44**, 5254–5257 (2019).
- Marrucci, L., Manzo, C. & Paparo, D. Optical spin-to-orbital angular momentum conversion in inhomogeneous anisotropic media. *Phys. Rev. Lett.* **96**, 163905 (2006).
- Su, W., Schrieffer, J. R. & Heeger, A. J. Solitons in polyacetylene. *Phys. Rev. Lett.* **42**, 1698 (1979).
- Asbóth, J. K. & Obuse, H. Bulk-boundary correspondence for chiral symmetric quantum walks. *Phys. Rev. B* **88**, 121406 (2013).
- Kitagawa, T., Berg, E., Rudner, M. & Demler, E. Topological characterization of periodically driven quantum systems. *Phys. Rev. B* **82**, 235114 (2010).
- Xiao, L. et al. Non-Hermitian bulk-boundary correspondence in quantum dynamics. *Nat. Phys.* **16**, 1 (2020).
- Xiao, L. et al. Observation of topological edge states in parity-time-symmetric quantum walks. *Nat. Phys.* **13**, 1117 (2017).
- Luo, X. W. et al. Synthetic-lattice enabled all-optical devices based on orbital angular momentum of light. *Nat. Commun.* **8**, 1–7 (2017).

Acknowledgements

We acknowledge the discussion with Ze-Di Cheng. This work was supported by the National Key Research and Development Program of China (Grant No. 2016YFA0302700),

the Innovation Program for Quantum Science and Technology (2021ZD0301400), the National Natural Science Foundation of China (Grants No. 11874343, 61725504, 61327901, 11974334, 11774335, 11821404 and U19A2075), the Key Research Program of Frontier Sciences, Chinese Academy of Sciences (CAS) (Grant No. QYZDY-SSW-SLH003), Science Foundation of the CAS (No. ZDRW-XH-2019-1), Anhui Initiative in Quantum Information Technologies (AHY060300 and AHY020100), the Fundamental Research Funds for the Central Universities (Grant No. WK2030380017 and WK2470000026).

Author contributions

M.Y. and Y.-W.L. experimented with the assistant of J.-S.X. and Z.H.L.; M.Y., H.-Q.Z. and Y.-J.H. contributed to the theoretical analysis with the help of Z.W.Z. and X.X. Z; J.-S.X., Y.-J.H., C.-F.L. and G.-C.G. supervised the project. All authors read the paper and discussed the results.

Competing interests

The authors declare no competing interests.

Additional information

Supplementary information The online version contains supplementary material available at <https://doi.org/10.1038/s41467-022-29779-3>.

Correspondence and requests for materials should be addressed to Jin-Shi Xu, Yong-Jian Han or Chuan-Feng Li.

Reprints and permission information is available at <http://www.nature.com/reprints>

Publisher's note Springer Nature remains neutral with regard to jurisdictional claims in published maps and institutional affiliations.



Open Access This article is licensed under a Creative Commons Attribution 4.0 International License, which permits use, sharing, adaptation, distribution and reproduction in any medium or format, as long as you give appropriate credit to the original author(s) and the source, provide a link to the Creative Commons license, and indicate if changes were made. The images or other third party material in this article are included in the article's Creative Commons license, unless indicated otherwise in a credit line to the material. If material is not included in the article's Creative Commons license and your intended use is not permitted by statutory regulation or exceeds the permitted use, you will need to obtain permission directly from the copyright holder. To view a copy of this license, visit <http://creativecommons.org/licenses/by/4.0/>.

© The Author(s) 2022